














Bolometric Hemispherical Albedo Map of Pluto from New Horizons Observations

Jason D. Hofgartner^{1,2} , Bonnie J. Buratti² , Ross A. Beyer^{3,4} , Kimberly Ennico⁴, Will M. Grundy^{5,6} , Carly J. A. Howett⁷,
Perianne E. Johnson⁸ , Tod R. Lauer⁹ , Catherine B. Olkin¹ , John R. Spencer¹ , S. Alan Stern¹ ,
Harold A. Weaver¹⁰ , and Leslie A. Young¹ 

¹ Southwest Research Institute, Boulder, CO 80302, USA; jason.hofgartner@swri.org

² Jet Propulsion Laboratory, California Institute of Technology, Pasadena, CA 91109, USA

³ Sagan Center at SETI Institute, Mountain View, CA 94043, USA

⁴ NASA Ames Research Center, Mountain View, CA 94043, USA

⁵ Lowell Observatory, Flagstaff, AZ 86001, USA

⁶ Northern Arizona University, Flagstaff, AZ 86011, USA

⁷ University of Oxford, Oxford OX1 3AZ, UK

⁸ University of Colorado Boulder, Boulder, CO 80309, USA

⁹ NSF's National Optical Infrared Astronomy Research Laboratory, Tucson, AZ 85719, USA¹¹

¹⁰ Johns Hopkins University, Applied Physics Laboratory, Laurel, MD 20723, USA

Received 2022 November 23; revised 2023 June 10; accepted 2023 June 28; published 2023 July 27

Abstract

The New Horizons encounter with the Pluto system revealed Pluto to have an extremely spatially variable surface with expansive dark, bright, and intermediate terrains, refractory and volatile ices, and ongoing/recent endogenous and exogenous processes. Albedo is useful for understanding volatile transport because it quantifies absorbed solar energy; albedo may also provide insights into surface processes. Four filters of the New Horizons LORRI and MVIC imagers are used to approximate the bolometric (flux-weighted, wavelength-integrated) albedo. The bolometric hemispherical albedo (local energy balance albedo) as a function of the incidence angle of the solar illumination is measured for both Cthulhu and Sputnik Planitia, which are extensive, extreme dark and extreme bright terrains on Pluto. For both terrains, the bolometric hemispherical albedo increases by $>30\%$ from 0° to 90° incidence. The incidence-angle-average bolometric hemispherical albedo of Cthulhu is 0.12 ± 0.01 , and that of Sputnik Planitia is 0.80 ± 0.06 , where uncertainties are estimates based on scatter from different photometric functional approximations. The bolometric Bond albedo (global energy balance albedo) of Cthulhu is 0.12 ± 0.01 , and that of Sputnik Planitia is 0.80 ± 0.07 . A map of Pluto's incidence-angle-average bolometric hemispherical albedo is produced. The incidence-angle-average bolometric hemispherical albedo, spatially averaged over areas north of $\approx 30^\circ$ S, is ≈ 0.54 . Pluto has three general albedo categories: (1) very low albedo southern equatorial terrains, including Cthulhu; (2) high-albedo terrains, which constitute most of Pluto's surface; and (3) very high albedo terrains, including Sputnik Planitia. Pluto's extraordinary albedo variability with location is also spatially sharp at some places.

Unified Astronomy Thesaurus concepts: [Pluto \(1267\)](#); [Surface photometry \(1670\)](#); [Photometry \(1234\)](#); [Albedo \(2321\)](#); [Planetary science \(1255\)](#)

1. Introduction

The NASA New Horizons encounter with the Pluto system in 2015 revealed Pluto to have an extraordinary range of surface albedos, abundant volatile and refractory ices, and complex geology from endogenous and exogenous processes (Stern et al. 2015). Pluto is an active world with ongoing convective and glacial resurfacing, seasonal volatile transport that includes nitrogen and methane cycles, and chemical processing by ionizing radiation (e.g., Gladstone et al. 2016; Grundy et al. 2016; Moore et al. 2016). Photometric properties of a surface, including albedo, are useful for constraining volatile transport by quantifying absorbed solar energy, as well as for providing insights into surface processes. For example, albedo measurements can contribute to relative estimates of

processing, mixing, temporal variability, and age for different terrains.

The New Horizons spacecraft flew by Pluto, and the hemisphere observed during closest approach by the spacecraft, hereafter called the encounter hemisphere, was approximately the anti-Charon hemisphere (hemisphere facing away from Pluto's moon Charon; a figure of the geometry is included in Olkin et al. 2017). The spacecraft approached Pluto from a Sun–Pluto–spacecraft angle (solar phase angle, α) asymptote of $\approx 15^\circ$, flew behind Pluto relative to the Sun (occultation, $\alpha \approx 180^\circ$), and departed toward an asymptote of $\approx 165^\circ$. Thus, most of Pluto's disk was illuminated during approach, but only a crescent of the surface (but more of the atmosphere) was illuminated during departure. Observations as the spacecraft approached and Pluto rotated resulted in improving spatial resolution in a westward direction until the best-resolution observations of the encounter hemisphere. The subsolar latitude on Pluto during the 2015 New Horizons encounter was 52° N and moving northward. Locations south of 38° S were in winter darkness (polar night) and were not observed, except by observations that utilized scattering from Pluto's atmospheric haze (Schenk et al. 2018) or Charon (Lauer et al. 2021). New

¹¹ The NSF's OIR Lab is operated by AURA, Inc. under cooperative agreement with NSF.

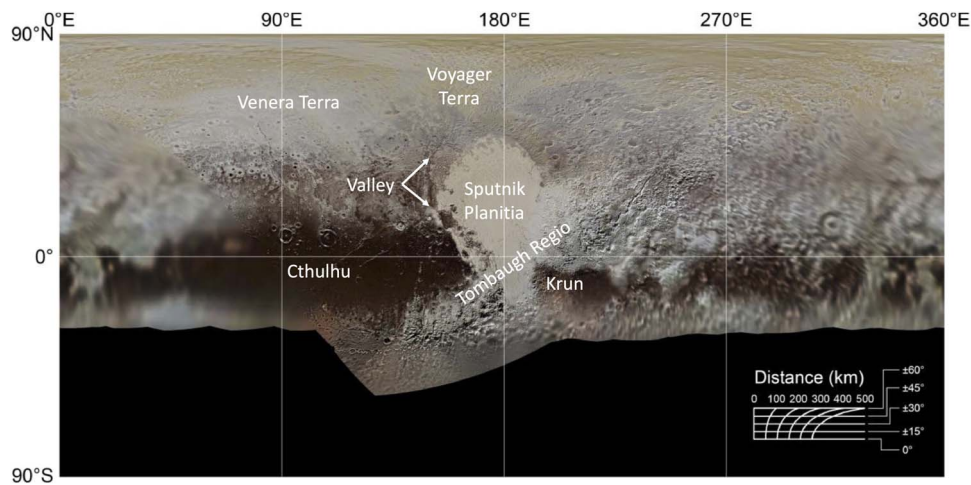


Figure 1. Pluto’s varied terrains. Terrains discussed are labeled. Some names are informal. Sputnik Planitia is a part of Tombaugh Regio. The Valley annotation indicates a relatively low albedo valley referred to in the Discussion section. The map is approximately longitudinally centered on the encounter hemisphere; colors are based on MVIC blue, red, and methane filters. Figure adapted from Schenk et al. (2018) with permission. Geographic coordinates are based on out-of-date ephemerides; longitude labels should be decreased by $\approx 1.5^\circ$ to become consistent with the current ephemerides used in this work.

Horizons images of Pluto include observations by the narrower-angle Long Range Reconnaissance Imager (LORRI; Cheng et al. 2008) and wider-angle Multispectral Visible Imaging Camera (MVIC; Reuter et al. 2008). LORRI has a single panchromatic filter, and MVIC has a panchromatic (Pan) filter, as well as four color filters (blue, red, near-infrared (NIR), and methane (CH₄)). The approximate bandpasses and pivot wavelengths of each filter are shown in Table 1. The radiometric, absolute error of calibrated observations of Pluto is $\approx 2\%$ for LORRI (Weaver et al. 2020), $< 1\%$ for all MVIC filters except the CH₄ filter, and $< 7\%$ for MVIC CH₄ (Howett et al. 2017).

Preliminary maps of normal reflectance and disk-resolved approximate Bond albedo, two photometric properties, were produced from a subset of LORRI observations of Pluto (Buratti et al. 2017). Consistent with predictions, from Earth-based observations, of large albedo variations with location (e.g., Buie et al. 2010), the preliminary maps indicate that albedo variations with location on Pluto are extreme, among the largest of all explored bodies in the solar system. An ≈ 1000 km diameter nitrogen, carbon monoxide, and methane ice sheet in a basin and centered at $\approx 180^\circ$ E, 30° N, called Sputnik Planitia (Figure 1), was found to be among Pluto’s brightest terrains. Southwest of Sputnik Planitia, an $\approx 3000 \times 500$ km region composed of water ice and other refractory material, which stretches over $\approx 150^\circ$ in longitude, informally called Cthulhu, is among the darkest terrains. The normal reflectance and disk-resolved approximate Bond albedo maps were preliminary and produced assuming that the change of scattered intensity by the surface with change in imaging geometry is identical for all terrains on Pluto. That assumption was reasonable to produce preliminary maps but is unsatisfactory for a world with such extraordinary albedo variations. We present a bolometric hemispherical albedo (i.e., energy albedo, equal to one minus absorption) map, which, among other improvements, does not make that approximation and also utilizes both LORRI and MVIC images.

In Section 2 we discuss and show the data used to measure the bolometric hemispherical albedos of Pluto. Section 3 defines the photometric function that describes the change of scattered intensity with change of imaging geometry and details

Table 1
Filters of New Horizons LORRI and MVIC Instruments (Cheng et al. 2008; Howett et al. 2017)

Instrument	Filter	Approximate Wave-length Range (nm)	Pivot Wave-length (nm)
LORRI	Panchromatic	350–850	608
MVIC	Panchromatic (Pan)	400–975	692
MVIC	Blue	400–550	492
MVIC	Red	540–700	624
MVIC	Near-infrared (NIR)	780–975	861
MVIC	Methane (CH ₄)	860–910	883

its application to Pluto. Section 4 provides the calculation of bolometric hemispherical albedo from the photometric function. Definitions of photometric properties and parameters are provided with their first use in Sections 2–4. A map of Pluto’s bolometric hemispherical albedo is presented in Section 5. It is interpreted and discussed in Section 6, and Section 7 summarizes conclusions.

2. Data

Reflectance (also called radiance factor) is defined here as I/F , where I is the scattered intensity from the surface and πF is the normally incident solar flux at the distance of the scattering surface. Reflectance varies owing to both intrinsic variations between surfaces and variations of imaging geometry. Imaging geometry is specified by the photometric angles: incidence, emission, and solar phase angle. Incidence angle, i , is the angle between the surface normal and surface–Sun vector. Emission angle, e , is the angle between the surface normal and surface–camera vector. Recall from above that solar phase angle, α , is the Sun–surface–observer angle. Normal reflectance is reflectance at $i=e=\alpha=0^\circ$; geometric albedo is disk-integrated reflectance at $\alpha=0^\circ$. An ideal photometric data set includes observations at all possible combinations of i , e , and α , so that the reflectance variation with imaging geometry is completely determined. Photometric data also improve with broader spectral and geographic coverage, as well as better spectral

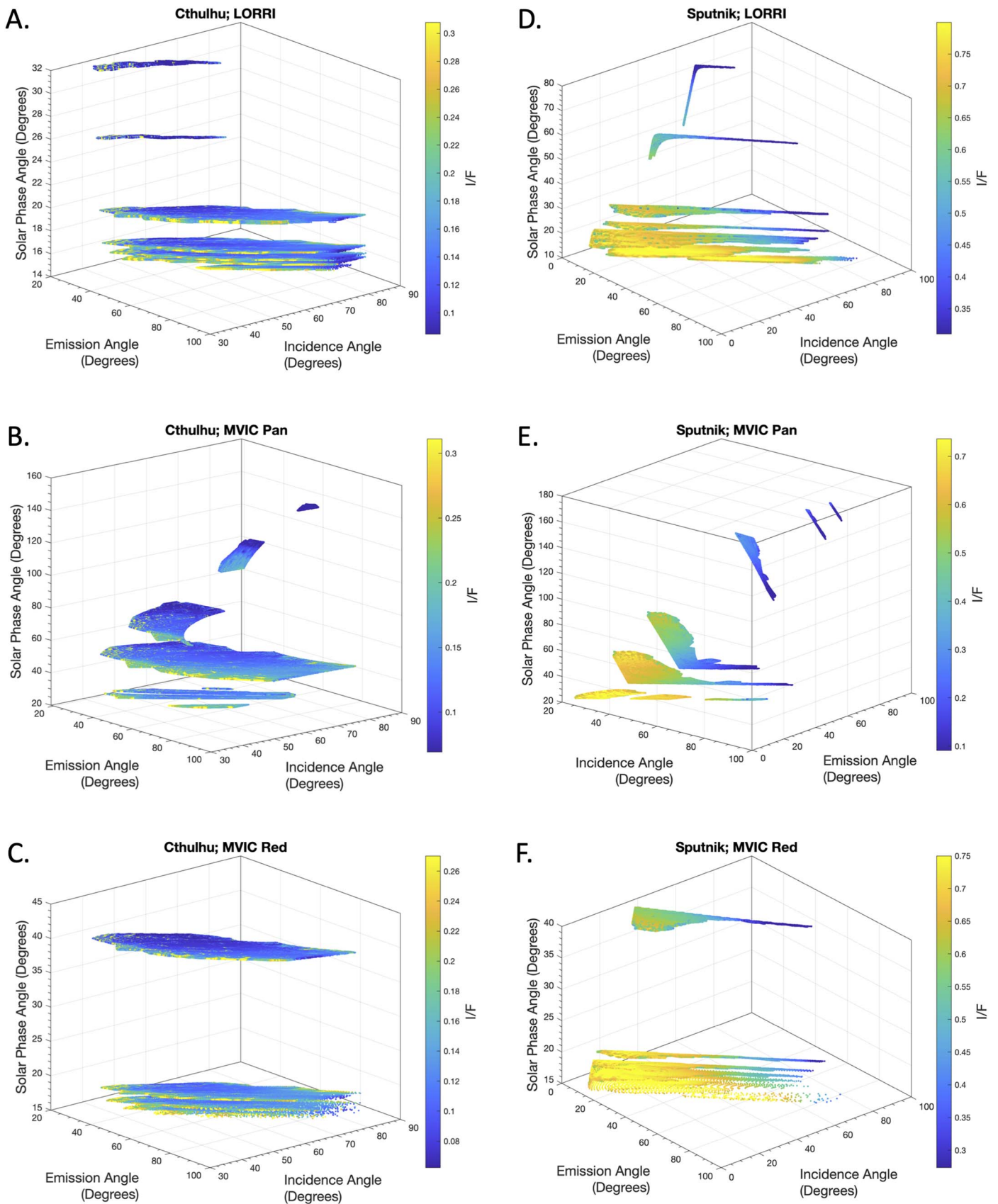


Figure 2. New Horizons data used for photometric analysis. MVIC color observations were always acquired as sequences that included all four color filters (blue, red, NIR, and CH4); only red filter data are shown because the photometric coverage is similar for the other three color filters. The data do not encompass every possible combination of the photometric angles. Cthulhu and Sputnik Planitia have similar but not identical coverage of photometric angles. Coverage varies among the LORRI, MVIC Pan, and MVIC color filters. The limits of the color bar, for each panel, are set at the 2.5 and 97.5 percentiles.

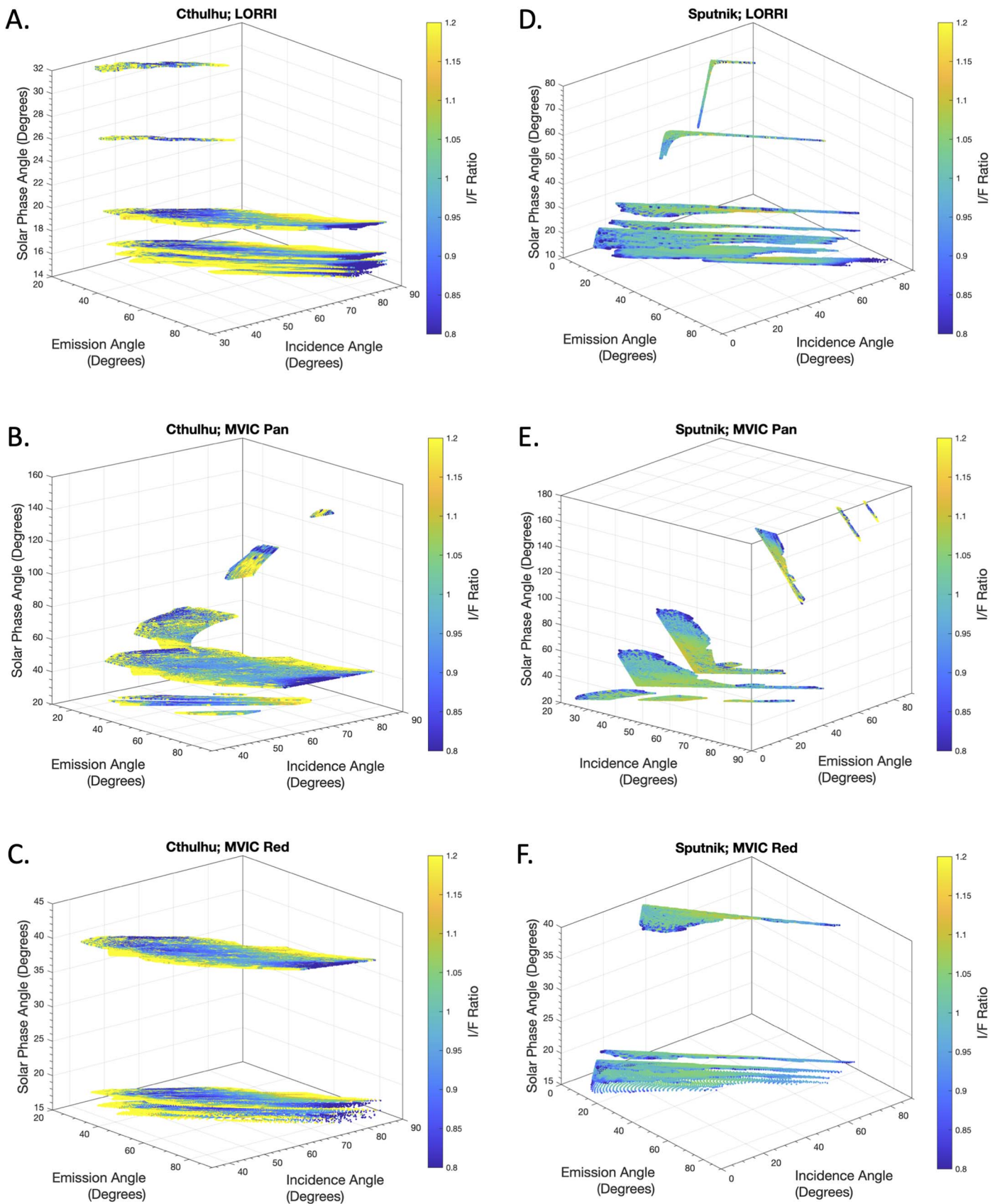


Figure 3. Ratios of New Horizons data of Pluto in Figure 2 to best-fit lunar-Lambert photometric functions. The best-fit lunar-Lambert functions approximately describe the observed photometric variation.

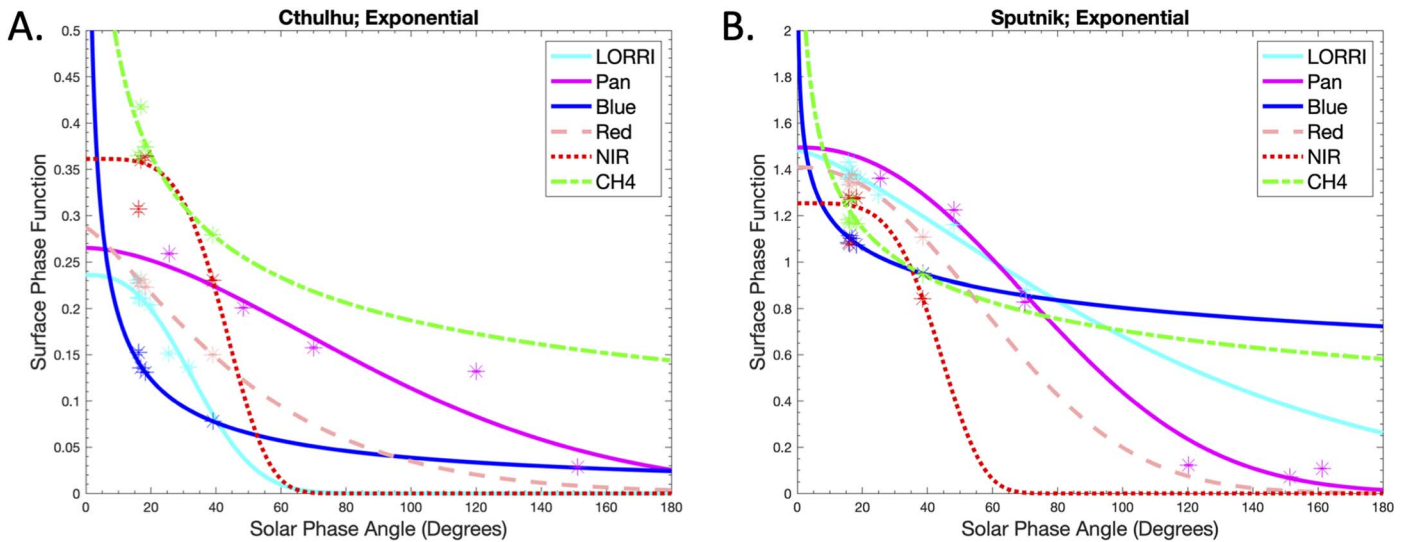


Figure 4. Surface phase function ($f(\alpha)$) best fits and best-fit three-parameter exponential functions to $f(\alpha)$ for Pluto’s Cthulhu and Sputnik Planitia. Solar phase angle (α) coverage is limited as in Figure 2. The 95% statistical confidence intervals of the $f(\alpha)$ best fits for each sequence are shown, but they are generally smaller than the symbols.

and spatial resolution. Photometric observations of Pluto from Earth are limited to $\alpha \lesssim 1.9^\circ$ and poor spatial resolution.

This research utilizes New Horizons LORRI and MVIC images, including all filters, to improve spectral coverage. The LORRI and MVIC filters extend across visible and NIR wavelengths (Table 1), including the wavelengths of greatest solar flux; are radiometrically calibrated (1%–7% absolute accuracy); and thus are appropriate for measuring bolometric (flux-weighted, wavelength-integrated) albedo. The New Horizons flyby resulted in a wide range of imaging geometries ($15^\circ \lesssim \alpha \lesssim 180^\circ$); however, that variation is generally accompanied by undesirable variations in spatial resolution and geographic coverage. Observations at intermediate solar phase angles are limited since they could only be acquired near closest approach, when the imaging geometry varied rapidly. As discussed below, numerous image sequences are utilized in this research, to increase coverage of all three photometric angles. The term “image sequence” refers here to a set of images acquired in rapid succession; images within a sequence have similar solar phase angles and spatial resolutions but may vary in geographic coverage.

Cthulhu and Sputnik Planitia are two expansive terrains on Pluto’s encounter hemisphere (Figure 1) and thus are among the best-imaged terrains for photometric analysis. In particular, they were imaged at a variety of photometric angles, including intermediate solar phase angles, with both LORRI and MVIC, and at New Horizons’ best spatial resolution. Moreover, they are reflectance extremes; Cthulhu is among Pluto’s darkest terrains, and Sputnik Planitia is among its brightest (Buratti et al. 2017). They therefore are representative of Pluto’s extraordinary albedo variations with location. Both are also relatively photometrically homogenous, as Cthulhu is likely blanketed by atmospheric deposits (Grundy et al. 2016; Moore et al. 2016; Fayolle et al. 2021) and Sputnik Planitia is likely mixed by convection (McKinnon et al. 2016; Morison et al. 2021). For the above reasons, we take Cthulhu and Sputnik Planitia as representative of Pluto’s albedo variability and focus our photometric analysis on these two terrains. Thus, both the low and high extremes are included but independently analyzed. It is assumed that each terrain has homogenous

Table 2

Best Fits for Lunar-Lambert A Parameter for New Horizons Observations of Pluto

Instrument and Filter	Cthulhu	Sputnik Planitia
LORRI	0.94	0.70
MVIC Pan	0.93	0.68
MVIC Blue	0.98	0.82
MVIC Red	0.97	0.69
MVIC NIR	0.91	0.63
MVIC CH4	0.89	0.61

Note. The 95% statistical uncertainty of all measurements is <0.01 .

photometric properties across its surface, which is observed to be approximately true.

Data for photometric analysis were selected as follows. Numerous image sequences are included to increase photometric coverage; in all cases all applicable images in a sequence are utilized. The solar phase angle varies slightly ($< 1^\circ$) with location on Pluto in each image, and sequences were selected to exclude any overlap of solar phase angle. Only sequences that contain ≥ 1000 pixels of at least one of Cthulhu or Sputnik Planitia are included. For MVIC observations, following the above criteria for data selection, the low- α limit of inclusion is set by coverage of Cthulhu/Sputnik and spatial resolution. The MVIC high- α limit is set by identification of the surface, which is not apparent in very high α and poor spatial resolution observations. For LORRI observations, an additional criterion is added: only sequences up to approximately one Pluto rotation (Pluto’s rotational period is ≈ 6.4 Earth-days) prior to closest approach are included, because earlier sequences have little difference of α but substantially poorer spatial resolution. The LORRI low- α limit of inclusion is set by coverage of Cthulhu/Sputnik and that additional criterion; all applicable images after Cthulhu/Sputnik rotated into New Horizons’ view approximately one Pluto rotation prior to closest approach are included. The LORRI high- α limit is based on satisfactory geolocation; for very high α sequences, little surface is observed and confidence of the geographic

location of the observed surface degrades. In total, >20 million pixels of Cthulhu and >59 million pixels of Sputnik Planitia are included.

All utilized images were processed using the USGS Integrated Software for Imagers and Spectrometers (ISIS) to determine geographic locations (i.e., add latitude and longitude), photometric angles (i , e , α), and calibrated reflectance (I/F). Pluto was assumed to be a sphere (Nimmo et al. 2017). The MVIC Pan sequence at $\alpha \approx 120^\circ$, called P_Photoslew, was deconvolved, to reduce smear, using techniques similar to those described in Weaver et al. (2016, 2020). Pixels of Cthulhu and Sputnik Planitia were identified, and the photometric parameters (I/F , i , e , α) for those pixels were extracted. The data are shown in Figure 2.

3. Photometric Function

A variety of photometric functions have been used to describe the reflectance of planetary surfaces as a function of imaging geometry (e.g., Hapke 2012). For New Horizons observations of Pluto, we use a linear combination of Lommel-Seeliger, also known as lunar, and Lambert photometric functions and refer to the combined function as the lunar-Lambert photometric function. The Lommel-Seeliger function is an analytic solution to the equations of radiative transfer for single scattering. The Lambert function describes perfectly diffuse scattering and is a good approximation of reflectance from multiple scattering. Thus, both single scattering and multiple scattering are considered in the empirical lunar-Lambert function. The lunar-Lambert function has been used to investigate several planetary surfaces (e.g., Buratti & Veverka 1983). It is appropriate for a limited data set because it has few parameters. The lunar-Lambert function was also used for preliminary New Horizons photometric maps of Pluto (Buratti et al. 2017) and for photometric analysis of New Horizons observations of Kuiper Belt object (486958) Arrokoth (Hofgartner et al. 2021). Another commonly used photometric function is the isotropic multiple-scattering approximation, also called the Hapke photometric function (e.g., Hapke 2012). The lunar-Lambert and Hapke photometric functions are similar in the limits of single scattering, low reflectance, and high reflectance (see the Appendix).

The lunar-Lambert photometric function is

$$\frac{I}{F} = A \frac{f(\alpha) \cos i}{\cos i + \cos e} + (1 - A) \cos i, \quad (1)$$

where I/F , i , e , and α , are the reflectance, incidence angle, emission angle, and solar phase angle, respectively, as defined above. The first term on the right-hand side of the equation is the Lommel–Seeliger (lunar, single scattering) photometric function, and the second term is the Lambert (diffuse, multiple scattering) function. The A parameter is empirical and depends on the relative contributions of the lunar and Lambert functions and the magnitude of the normal reflectance, and $f(\alpha)$ is the surface phase function, which depends on physical properties such as surface roughness, the compaction state, and the single-scattering phase function. We note that A is not the partition between the lunar and Lambert functions because it also incorporates the magnitude of the surface reflectance (e.g., $A = 0.5$ does not imply that the lunar and Lambertian terms contribute equally to the I/F ; McEwen 1986). A could be allowed to depend on α ; however, in that case the second term

is no longer the Lambertian function for diffuse scattering. Equation (1) is valid for $0^\circ \leq i \leq 90^\circ$ and $0^\circ \leq e \leq 90^\circ$; otherwise, $I/F = 0$.

Haze in Pluto’s atmosphere was imaged by both LORRI and MVIC, and it is most apparent in high solar phase angle images (e.g., Stern et al. 2015; Kutsop et al. 2021). Haze extinction (scattering plus absorption) affects the measured I/F ; however, Pluto’s surface dominates Pluto’s disk-integrated (surface plus atmosphere) I/F at $0^\circ \leq \alpha \lesssim 160^\circ$ (Hillier et al. 2021). Furthermore, surface features are readily recognizable in all utilized images ($\alpha \leq 161^\circ$), suggesting that the surface likewise dominates the disk-resolved I/F over an even greater range of α for pixels of the surface (recall that only pixels of the surface of Cthulhu or Sputnik Planitia are included in Figure 2), as expected. Therefore, extinction from Pluto’s atmosphere, including its haze, is ignored, and the associated error is greatest for observations at the greatest α .

The function in Equation (1) was fit to the data in Figure 2 and the complementing MVIC color data that are not shown in the figure, separately for Cthulhu and Sputnik Planitia, for each filter. The $f(\alpha)$ parameter was fit for each sequence by averaging over the small variations of α ($< 1^\circ$) with location within a sequence. The fit residuals were weighted by the inverse of I/F , since I/F generally decreases with increasing α , and we argue that a good relative fit to each measurement is a better description of the photometric variation than a good absolute fit to all measurements. Ratios of data to best-fit functions are shown in Figure 3, the best fits for A are given in Table 2, and the best fits for $f(\alpha)$ are shown in Figure 4.

The ratios shown in Figure 3 are approximately equal to unity, indicating that the best-fit lunar-Lambert functions approximately describe the observed photometric variation. Ratios near the incidence angle limits of Cthulhu’s photometric coverage are typically > 1 , which suggests that the northern and southern margins of Cthulhu are intrinsically brighter than its central latitudes, consistent with the interpretation that Cthulhu is blanketed by dark material and that material is less concentrated away from Cthulhu’s central latitude. The function predicts a relatively sharp increase of I/F at very large emission angles that is not observed (ratios < 1 at $e \approx 90^\circ$), but otherwise the best-fit functions are similar to the observations. Observed differences between Cthulhu and Sputnik Planitia, observed differences among filters, and observed variability with all three photometric angles are approximately described by the best-fit functions. We also checked the residuals of the best fits subtracted from the data (similar to Hofgartner et al. 2021) and did not identify trends with photometric angles, which further increases confidence in the best-fit functions.

The best-fit lunar-Lambert A parameters in Table 2 have a similar trend to that of icy satellites of Jupiter and Saturn (Buratti & Veverka 1983, 1984; Buratti 1984). For high-albedo icy satellites such as Mimas and Tethys, A ranges from 0.61 to 0.77 for $\alpha < 30^\circ$, but for lower albedo regions, on Dione and Rhea, for example, A is 0.96–0.98.

A variety of functions have been proposed for $f(\alpha)$, with varying degrees of complexity and success (e.g., Hapke 2012). A three-parameter exponential function of the form

$$f(\alpha) = c_1 e^{c_2 \alpha^{c_3}}, \quad (2)$$

where c_1 , c_2 , and c_3 are empirical parameters, was found to provide a good fit to New Horizons and Hubble Space

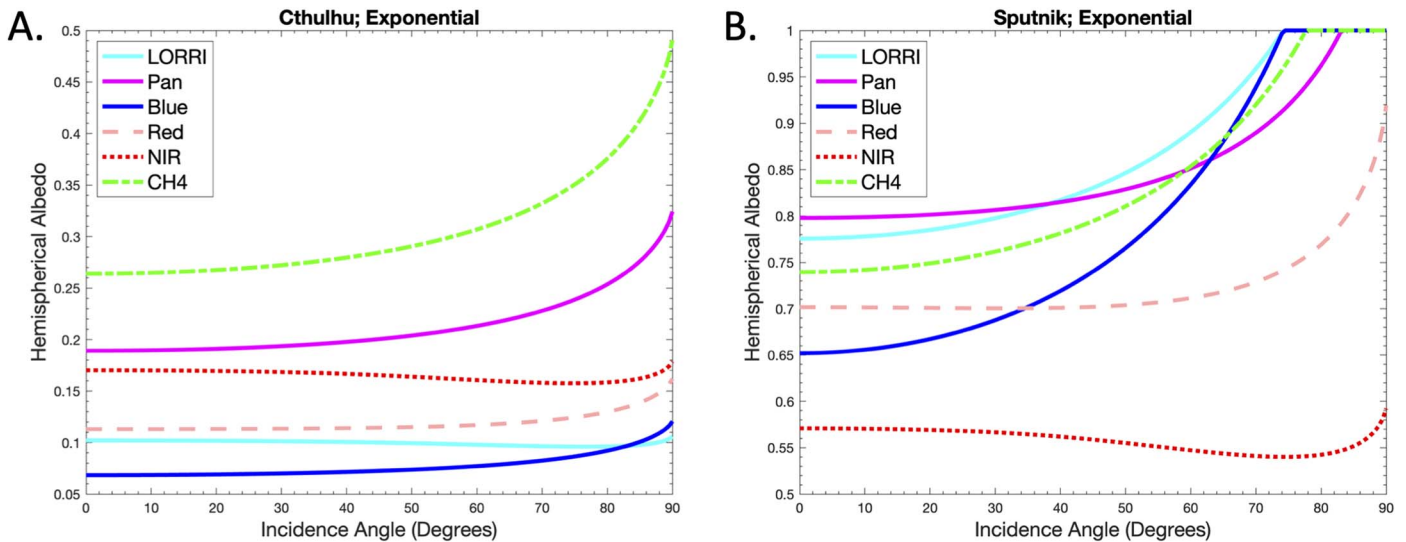


Figure 5. Hemispherical albedos as a function of incidence angle for best-fit Cthulhu and Sputnik Planitia lunar-Lambert photometric functions. Hemispherical albedos of Cthulhu and Sputnik Planitia are consistent with their redder and whiter colors (e.g., Protopa et al. 2020). The physical upper limit of unity is enforced as necessary.

Telescope observations of Arrokoth (Hofgartner et al. 2021). As shown in Figure 4, it also satisfactorily fits the $f(\alpha)$ for Pluto. We also considered one-term and two-term Henyey–Greenstein functions, as well as two-term and three-term Legendre polynomials. Note that Henyey–Greenstein functions and Legendre polynomials have also been used to approximate the single-scattering phase function (e.g., Hapke 2012), whereas for this research they were considered for the surface phase function, $f(\alpha)$, which can resemble the single-scattering phase function (see the Appendix). The shape of the $f(\alpha)$ fit varies with functional form, but as discussed below, we find that for Pluto the hemispherical and Bond albedos, which depend on integrals of $f(\alpha)$, are relatively insensitive to functional form. This weak sensitivity increases confidence in the albedo results, and the variation with functional form offers one estimate of uncertainty.

Surface reflectance (I/F) can vary dramatically with solar phase angle near opposition ($\alpha \approx 0$; e.g., Hapke 2012). New Horizons, however, did not observe Pluto at $\alpha \lesssim 15^\circ$. Thus, extrapolations of the best-fit functions for $f(\alpha)$ may not be good approximations near $\alpha = 0$. Normal reflectance (I/F at $i = e = \alpha = 0$, as defined earlier) is therefore also poorly approximated by the best-fit lunar-Lambert functions; hence, it is not reported. Earth-based measurements at $0 \lesssim \alpha \lesssim 1.8^\circ$ have been acquired (e.g., Buratti et al. 2015, 2021; Verbiscer et al. 2022), but they do not resolve Cthulhu and Sputnik Planitia. Conversely, as discussed further below, we find that hemispherical albedo, which is the ratio of total power scattered by a surface to the incident power, within a given spectral range, depends only weakly on $f(0)$. Similarly, Bond albedo, which is the ratio of total power scattered by a planetary body to the incident power (Bond albedo is disk integrated, whereas hemispherical albedo is disk resolved), within a given spectral range, is almost independent of dramatic variations near opposition (e.g., Hillier et al. 2021). Hemispherical albedo is a crucial parameter for thermal considerations and is the focus of this research.

The MVIC NIR $f(\alpha)$ in Figure 4 have significantly greater scatter at low solar phase angles than that of other filters.

Calibration observations indicate that MVIC NIR measurements have a substantially greater drift than measurements with other filters (Howett et al. 2017). The $f(\alpha)$ variability in Figure 4 suggests that the MVIC NIR drift may affect Pluto encounter observations. There are insufficient calibration observations to confidently, for absolute photometric analysis, remove this drift from Pluto encounter observations. We report results for the MVIC NIR filter, but due to the uncalibrated drift, we exclude this filter from synthesis measurements below.

4. Albedos

4.1. Hemispherical Albedo

Hemispherical albedo, as defined above, is the ratio of total power scattered by a surface, where “total” refers to integration over all emission angles, to incident power. Bolometric hemispherical albedo is the flux-weighted, wavelength-integrated ratio and is crucial for understanding the thermal behavior of a surface. The lunar-Lambert photometric function describes the scattered radiation for all geometries; thus, the total scattered power can be determined by integrating the function over the emission hemisphere. The equation for hemispherical albedo is

$$a(i) = \frac{\int_0^{\frac{\pi}{2}} \int_0^{2\pi} I(\theta, \phi) \cos \theta \sin \theta d\phi d\theta}{\pi F \cos i}, \quad (3)$$

where $a(i)$ is the hemispherical albedo, θ and ϕ are the spherical polar angles (θ is equivalent to the emission angle, e), and the other variables (i , I , and F) are consistent with the definitions in previous sections. Note that Equation (3) indicates that the hemispherical albedo of a general surface depends on the incidence angle of the incident power (Squyres & Veverka 1982).

The hemispherical albedo of the Lambertian component of the lunar-Lambert photometric function is analytic and equal to the normal reflectance of the Lambertian component, $1 - A$, independent of incidence angle. The Lommel–Seeliger (lunar) component was numerically integrated (intermediate steps are

Table 3
Hemispherical Albedos for Best-fit Cthulhu and Sputnik Planitia Lunar-Lambert Photometric Functions

Instrument and Filter	Approximate Wavelength Range (nm)	Pivot Wavelength (nm)	Incidence-angle-average Hemispherical Albedo		Cosine-weighted-average Hemispherical Albedo	
			Cthulhu	Sputnik Planitia	Cthulhu	Sputnik Planitia
LORRI	350–850	608	0.10	0.86	0.10	0.82
MVIC Pan	400–975	692	0.21	0.85	0.20	0.82
MVIC Blue	400–550	492	0.08	0.78	0.07	0.72
MVIC Red	540–700	624	0.12	0.72	0.11	0.70
MVIC NIR	780–975	861	0.16	0.56	0.17	0.56
MVIC CH4	860–910	883	0.30	0.83	0.28	0.78

Note. Hemispherical albedos of Cthulhu and Sputnik Planitia are consistent with their redder and whiter colors (e.g., Protopapa et al. 2020). Estimated uncertainty varies with terrain and filter from negligible to 38%, with an average of <20%.

given in Hofgartner et al. 2021), and the summed lunar-Lambert results are shown in Figure 5. The Lommel–Seeliger component is also analytic for the specific case where $f(\alpha)$ is a two-term Legendre polynomial and the polynomial is greater than or equal to zero at all solar phase angles ($f(\alpha) \geq 0$ by definition; in some cases this is true for the best-fit two-term Legendre polynomial; however, in other cases it is forced when the polynomial would otherwise be ≤ 0), and we verified that the numerical result is equal to the analytic result in this special case (among other checks; Hofgartner et al. 2021). The integral of the best-fit lunar-Lambert function exceeds unity at very high incidence angles for some filters for Sputnik Planitia; unity is the physical upper limit for conservation of energy, so whenever the integral exceeds unity, the hemispherical albedo is truncated to unity. Note that a hemispherical albedo of greater than unity is temporarily possible in the case of exotic phenomena such as stimulated emission; however, we consider imperfections in the photometric function to be much more likely, for measured hemispherical albedos exceeding unity, than such phenomena for average Sputnik Planitia.

The incidence-angle-average hemispherical albedos and cosine-weighted-average hemispherical albedos ($\int a(i) \cos(i) di / \int \cos(i) di$) are provided in Table 3. We estimate the uncertainty of each hemispherical albedo from the uncertainty of $f(\alpha)$ at α far from New Horizons observations (Figure 4) using the scatter from different functional forms (exponential, Henyey–Greenstein, and Legendre) for $f(\alpha)$. We argue that this scatter provides a better estimate than the statistical uncertainty, based on the uncertainties of the best-fit $f(\alpha)$, of the adopted three-parameter exponential function, because it better incorporates the uncertainty at α far from New Horizons observations. The scatter varies with terrain and filter from negligible to 38%, with an average of <20%. Since this scatter can be much greater than other uncertainties, hereafter the maximum scatter from different functional forms for $f(\alpha)$ is used to estimate uncertainty.

4.2. Bond Albedo

Bond albedo is the ratio of the total power scattered by a planetary body to the incident power; it is different from hemispherical albedo in that it is disk integrated. The Bond albedo of the best-fit Cthulhu or Sputnik Planitia photometric function is the Bond albedo of a hypothetical planet everywhere covered by Cthulhu or Sputnik Planitia. The Bond albedo of a uniform sphere is independent of incidence angle. The Lambertian component of the lunar-Lambert photometric

Table 4
Bond Albedos for Best-fit Cthulhu and Sputnik Planitia Lunar-Lambert Photometric Functions

Instrument and Filter	Approximate Wavelength Range (nm)	Pivot Wavelength (nm)	Bond Albedo	
			Cthulhu	Sputnik Planitia
LORRI	350–850	608	0.10	0.86
MVIC Pan	400–975	692	0.21	0.84
MVIC Blue	400–550	492	0.07	0.78
MVIC Red	540–700	624	0.12	0.71
MVIC NIR	780–975	861	0.16	0.56
MVIC CH4	860–910	883	0.30	0.82

Note. Estimated uncertainty varies with terrain and filter from negligible to 31%, with an average of <20%.

function has a spherical Bond albedo of $1 - A$. The lunar component of the spherical Bond albedo can be numerically calculated (e.g., Hofgartner et al. 2021). The Bond albedos of the best-fit Cthulhu and Sputnik Planitia photometric functions are given in Table 4. The estimated uncertainty, based on the scatter from different functional forms for $f(\alpha)$ (dominant uncertainty), varies with terrain and filter from negligible to 31%, with an average of <20%. Pluto’s Bond albedo for each MVIC color filter was reported (Hillier et al. 2021), and, as expected, its Bond albedos are between those of its extreme terrains, except for the MVIC NIR filter, likely due to the drift discussed above.

4.3. Bolometric Hemispherical Albedo and Bolometric Bond Albedo

Bolometric albedo is the flux-weighted, wavelength-integrated albedo; bolometric hemispherical albedo is the energy balance albedo of a surface, equal to one minus absorption. The equation for bolometric hemispherical albedo is

$$a_{\text{Bolo}} = \frac{\int_0^\infty a(\lambda)F(\lambda)d\lambda}{\int_0^\infty F(\lambda)d\lambda}, \quad (4)$$

where a_{Bolo} is the bolometric hemispherical albedo, λ is wavelength, and the other variables (a and F) were defined previously. We approximate bolometric albedo with a summation of albedos from available filters using the filter pivot wavelengths and solar flux at those wavelengths. The measurements in Colina et al. (1996) of the solar flux as a

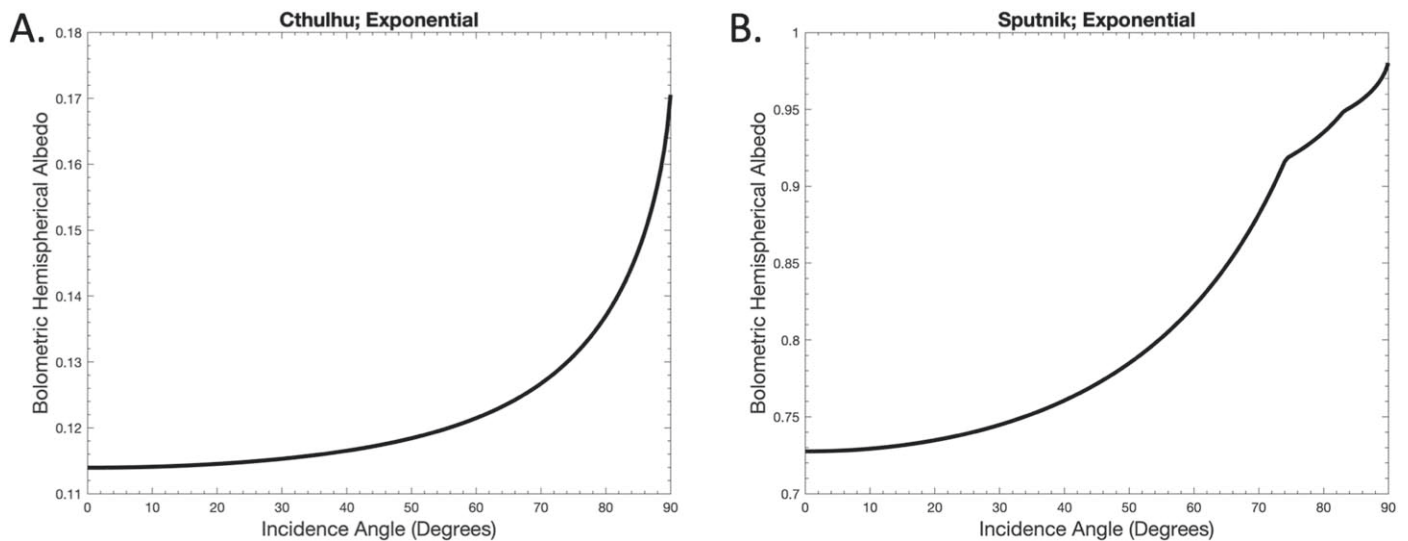


Figure 6. Bolometric hemispherical albedo of Pluto’s Cthulhu and Sputnik Planitia. Bolometric hemispherical albedo is approximated using best-fit photometric functions for the New Horizons LORRI panchromatic and MVIC panchromatic, blue, and red filters and the solar fluxes at their pivot wavelengths.

Table 5
Bolometric Albedos of Pluto’s Cthulhu and Sputnik Planitia

Terrain	Incidence-angle-average Bolometric Hemispherical Albedo	Cosine-weighted-average Bolometric Hemispherical Albedo	Bolometric Bond Albedo
Cthulhu	0.12 ± 0.01	0.12 ± 0.02	0.12 ± 0.01
Sputnik Planitia	0.80 ± 0.06	0.76 ± 0.04	0.80 ± 0.07

Note. Bolometric albedo is approximated using best-fit photometric functions for the New Horizons LORRI panchromatic and MVIC panchromatic, blue, and red filters and the solar fluxes at their pivot wavelengths. Uncertainties are estimates based on the scatter from different photometric functional forms.

function of wavelength are used. We report results for both the MVIC NIR and CH₄ filters above but exclude them from the calculation for bolometric albedo. As discussed above, the MVIC NIR observations have a drift that may be affecting results for that filter (Figure 4). The MVIC CH₄ filter was designed for a specific methane absorption band; it has a much narrower bandpass than the other filters and consequently has lower signal-to-noise ratios, in addition to greater absolute uncertainty. Thus, bolometric albedo is approximated with a summation of the LORRI panchromatic and MVIC panchromatic, blue, and red filter results. Bolometric Bond albedo can be calculated using the same formalism (i.e., Equation (4) with Bond albedo substituted for hemispherical albedo).

The bolometric hemispherical albedos for the best-fit Cthulhu and Sputnik Planitia photometric functions are plotted as a function of incidence angle in Figure 6. The incidence-angle-average and cosine-weighted-average bolometric hemispherical albedos, as well as the bolometric Bond albedos, are provided in Table 5. The uncertainties are estimates from the difference between results for a three-parameter exponential function for $f(\alpha)$ and results for a one-term Henyey–Greenstein function or two-term Legendre polynomial. The greatest absolute difference between the exponential and Henyey–Greenstein and exponential and Legendre results is used as the estimate for both the lower and upper uncertainties. As discussed previously, the albedo uncertainty is dominated by the uncertainty of the photometric parameter $f(\alpha)$, and we consider the estimates provided to be more representative of the true uncertainty than the statistical uncertainty.

The reflectances in Figure 2 and complementing MVIC color reflectances were calculated using the Pluto radiometric calibrations for LORRI and MVIC (called keywords in Weaver et al. 2020 and Howett et al. 2017). The LORRI and MVIC radiometric calibrations vary with the spectral energy distribution of the target (Weaver et al. 2020; Howett et al. 2017), and thus differences between the adopted Pluto spectrum and spectra of Cthulhu and Sputnik Planitia were implicitly ignored. To investigate the sensitivity of the bolometric albedos to the radiometric calibration, separate calibrations for each terrain were also considered. Cthulhu and Sputnik Planitia are not resolved by Earth-based observations, so their spectral energy distributions were iteratively approximated using New Horizons observations. Their spectral albedos (albedos multiplied by solar spectral energy distribution in calculation of radiometric calibration (Weaver et al. 2020; Howett et al. 2017) at the LORRI and MVIC pivot wavelengths were approximated by the corresponding incidence-angle-average hemispherical albedos (Table 3). Approximate spectra were generated by linear interpolation between pivot wavelengths. The MVIC NIR filter was excluded owing to the drift discussed above. Spectral albedos at wavelengths shorter than the pivot wavelength of the MVIC blue filter (shortest pivot wavelength) were approximated by extrapolation of a linear fit to the MVIC blue and LORRI albedos (two shortest pivot wavelengths). Spectral albedos at wavelengths longer than the MVIC CH₄ pivot wavelength (longest pivot wavelength) were approximated by a constant equal to the MVIC CH₄ albedo. Radiometric calibrations for each filter were calculated using these approximate spectra following the methods described in Weaver et al. (2020) and Howett et al. (2017).

Reflectances were then calculated using the newly determined radiometric calibrations, and then the analyses described in Section 3 and this section were repeated, resulting in another iteration of hemispherical albedos and approximate spectra. If the MVIC blue spectral albedo exceeded that of LORRI, spectral albedos at wavelengths shorter than the MVIC blue pivot wavelength were approximated by a constant equal to the MVIC blue albedo, rather than a linear fit to the MVIC blue and LORRI albedos. After six iterations, the bolometric incidence-angle-average hemispherical albedo of Cthulhu was 0.11 ± 0.01 (from 0.12 ± 0.01 ; Table 5), and that of Sputnik Planitia was 0.76 ± 0.05 (from 0.80 ± 0.06). The bolometric Bond albedo of Cthulhu was 0.11 ± 0.02 (from 0.12 ± 0.01), and that of Sputnik Planitia was 0.76 ± 0.05 (from 0.80 ± 0.07). All four bolometric albedos remained within their uncertainties throughout all iterations. All changes of the bolometric albedos between successive iterations were always by ≤ 0.01 . The bolometric incidence-angle-average hemispherical albedos of both terrains did not change (within rounding to hundredths) between the fifth and sixth iterations, and likewise for the bolometric Bond albedo of Cthulhu, which suggests nearing convergence. To further investigate the sensitivity of the bolometric albedos to the radiometric calibration, the Pholus (extremely red spectrum) radiometric calibration was considered for Cthulhu, and the solar (constant spectrum) radiometric calibration was considered for Sputnik Planitia (Weaver et al. 2020; Howett et al. 2017). For these calibrations, the bolometric incidence-angle-average hemispherical albedo and bolometric Bond albedo of Cthulhu are 0.11 ± 0.01 , and those of Sputnik Planitia are 0.79 ± 0.06 and 0.79 ± 0.07 . The small variations of the bolometric albedos among all of the above calibrations increase confidence that calibration uncertainties are small. We adopt the results based on the Pluto radiometric calibration (i.e., first iteration) as our measurements of the albedos, and we note again that the bolometric albedos are weakly sensitive to this choice.

5. Map

Pluto's extreme albedo variations with location can be fully presented with a map. A map should also facilitate more realistic simulations of Pluto's complex seasonal volatile transport, as well as further geologic interpretation. We produce a map of Pluto's incidence-angle-average bolometric hemispherical albedo by approximating regions of intermediate reflectance as a linear combination of reflectance low (Cthulhu) and high (Sputnik Planitia) extreme terrains. Thus, Pluto's extraordinary albedo range is well characterized in the map. Terrains with intermediate reflectance, however, are approximately characterized, in part due to limitations of the available photometric data.

To calculate the relative weights for Cthulhu and Sputnik Planitia for the linear combination, the calibrated I/F and photometric angles i , e , and α are extracted, from observations, for each and every illuminated location. The weights are calculated using the best-fit photometric functions for Cthulhu and Sputnik Planitia with the following equations:

$$\frac{I}{F} = (1 - W) \frac{I}{F_{C,\text{pred}}} + W \frac{I}{F_{S,\text{pred}}} \quad \text{for} \quad \frac{I}{F_{C,\text{pred}}} \leq \frac{I}{F} \leq \frac{I}{F_{S,\text{pred}}} \quad (5)$$

$$\frac{I}{F} = W \frac{I}{F_{S,\text{pred}}} \quad \text{for} \quad \frac{I}{F} > \frac{I}{F_{S,\text{pred}}} \quad (6)$$

$$\frac{I}{F} = -W \frac{I}{F_{C,\text{pred}}} \quad \text{for} \quad \frac{I}{F} < \frac{I}{F_{C,\text{pred}}}, \quad (7)$$

where I/F is the observed reflectance as defined previously, $I/F_{C,\text{pred}}$ is the predicted reflectance for Cthulhu when observed at the same photometric angles (i.e., the reflectance of the best-fit photometric function for Cthulhu), $I/F_{S,\text{pred}}$ is the predicted reflectance for Sputnik Planitia when observed at the same photometric angles, and W is the weight factor. In words, intermediate-reflectance locations are approximated as a combination of some amount of Cthulhu and Sputnik Planitia, while locations brighter than average Sputnik Planitia have a weight of greater than unity for average Sputnik Planitia and zero for average Cthulhu, and locations darker than average Cthulhu have an absolute weight of less than unity for average Cthulhu and zero for average Sputnik Planitia. The negative sign in Equation (7) is included to easily distinguish weights calculated using Equation (7) from those calculated using Equation (5). The calculated weight for each location is then used to approximate the incidence-angle-average bolometric hemispherical albedo of that location as

$$\overline{a_{\text{Bolo}}} = (1 - W) \overline{a_{C,\text{Bolo}}} + W \overline{a_{S,\text{Bolo}}} \quad \text{for} \quad 0 \leq W \leq 1 \quad (8)$$

$$\overline{a_{\text{Bolo}}} = W \overline{a_{S,\text{Bolo}}} \quad \text{for} \quad W > 1 \quad (9)$$

$$\overline{a_{\text{Bolo}}} = -W \overline{a_{C,\text{Bolo}}} \quad \text{for} \quad W < 0, \quad (10)$$

where $\overline{a_{\text{Bolo}}}$ is the incidence-angle-average bolometric hemispherical albedo, W is as defined above, and $\overline{a_{C,\text{Bolo}}}$ and $\overline{a_{S,\text{Bolo}}}$ are the incidence-angle-average bolometric hemispherical albedos of Cthulhu and Sputnik Planitia, respectively (the calculated albedos in Section 4 from the best-fit photometric functions).

The linear combination calculations of Equations (5)–(10) are implemented for each pixel in an image, and then images are mosaicked to produce a map. As discussed in earlier sections, the New Horizons flyby resulted in variations of image spatial resolution with geographic location. To choose image sequences for a mosaic of all illuminated regions on Pluto, which is a different purpose than the data selection described in Section 2 (which was focused on comprehensive photometric coverage of Cthulhu and Sputnik Planitia), we follow the approach of Hofgartner et al. (2018). In summary, P_LORRI, an image sequence with a pixel scale of ≈ 850 m, is used for the encounter hemisphere, and additional image sequences for other regions are selected such that the ratio of the pixel scales between successive utilized sequences is $\lesssim 2$ and Pluto's rotation between successive utilized sequences is $\lesssim 45^\circ$. Only LORRI images are used for the mosaic; recall, however, that MVIC information is included because $\overline{a_{C,\text{Bolo}}}$ and $\overline{a_{S,\text{Bolo}}}$ are determined from LORRI and MVIC observations, as described in previous sections. Selected sequences are mosaicked with better spatial resolution images overlaying worse spatial resolution images. Pixels with $e > 75^\circ$ and/or $i > 85^\circ$ are excluded, since the lunar-Lambert photometric function is more sensitive to small errors of these angles in the excluded regimes, and, as discussed above, the photometric function does not satisfactorily predict reflectance at very high emission angles. Underlying, worse spatial resolution images fill in trimmed pixels. Figure 7 is an equirectangular map of Pluto's incidence-angle-average bolometric hemispherical albedo, and Figure 8 is a polar stereographic projection of the north polar region.

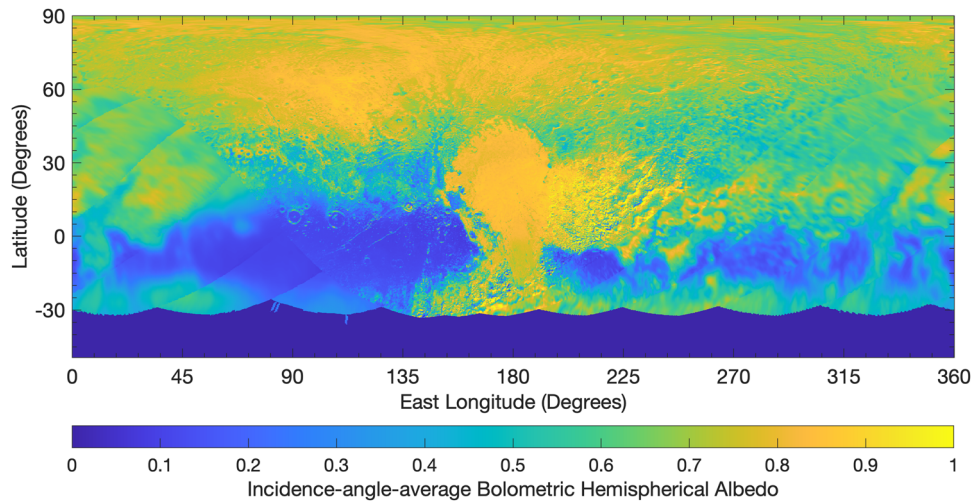


Figure 7. Incidence-angle-average bolometric hemispherical albedo map of Pluto. The map was produced using the best-fit photometric functions for Cthulhu and Sputnik Planitia as representative of low- and high-reflectance regions and by approximating intermediate-reflectance regions as a linear combination of these two extremes. New Horizons LORRI panchromatic and MVIC panchromatic, blue, and red observations were used to approximate bolometric albedo. Regions south of $\approx 38^\circ$ S were in winter darkness (polar night). The map projection is equirectangular.

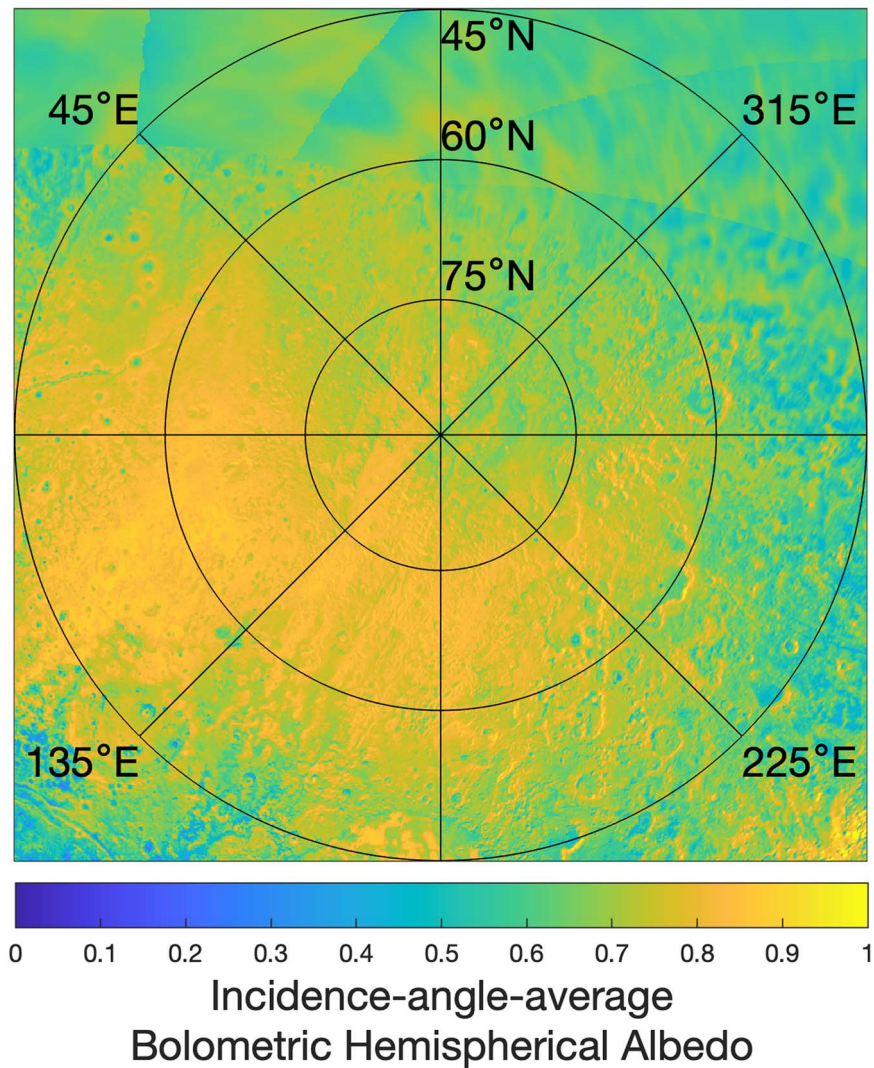


Figure 8. North polar stereographic projection of incidence-angle-average bolometric hemispherical albedo map of Pluto. Aside from the change of projection, the map is the same as in Figure 7.

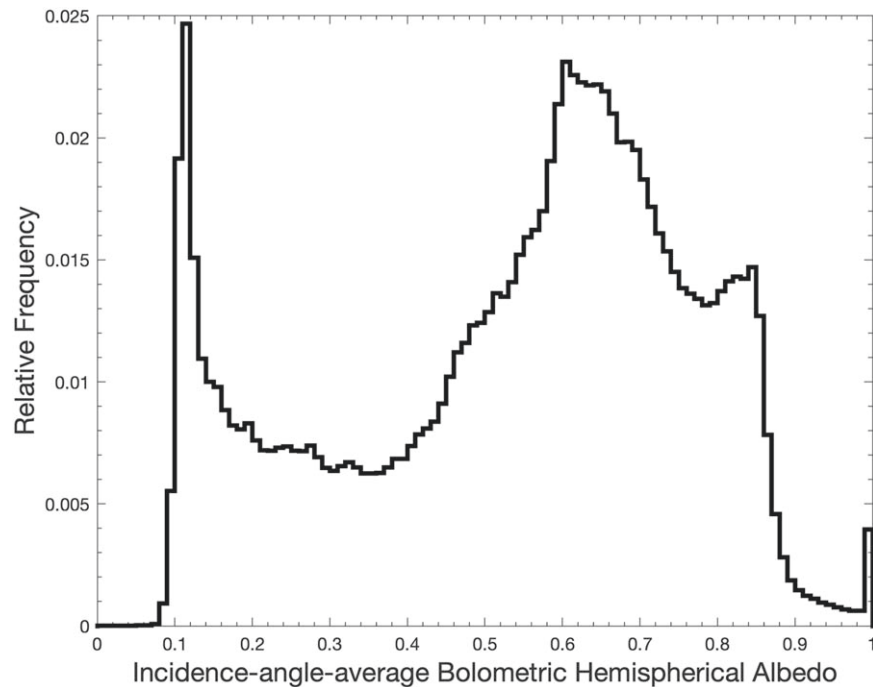


Figure 9. Histogram of incidence-angle-average bolometric hemispherical albedo of observed regions on Pluto. Pluto has three general albedo categories: (1) very low albedo southern equatorial terrains, including Cthulhu (mode of ≈ 0.1 , relatively narrow distribution); (2) high-albedo terrains that constitute most of Pluto’s surface (mode of ≈ 0.6 , distribution is much broader than that of the other two categories); and (3) very high albedo terrains, including Sputnik Planitia, East Tombaugh Regio, Venera Terra, and Voyager Terra (mode of ≈ 0.85 , relatively narrow distribution). Unity is the physical upper limit of bolometric hemispherical albedo in the absence of exotic phenomena, and the bin that includes unity has a spike owing to truncation of measurements that would otherwise exceed unity.

6. Discussion

Our incidence-angle-average bolometric hemispherical albedo map is qualitatively similar to the preliminary disk-resolved approximate Bond albedo map produced after the New Horizons encounter (Buratti et al. 2017). Pluto has an extraordinary range of bolometric hemispherical albedos. Venera Terra, Voyager Terra, and Tombaugh Regio, which includes Sputnik Planitia and glaciated highlands to its east (Figure 1), have very large bolometric hemispherical albedos that approach unity. The southern equatorial region, in contrast, is dominated by much lower albedo terrains, including Cthulhu and Krun. A histogram of Pluto’s measured incidence-angle-average bolometric hemispherical albedos is shown in Figure 9. The histogram was produced from an equal-area projection (the projections of Figures 7 and 8 do not conserve area). The incidence-angle-average bolometric hemispherical albedo of Pluto, spatially averaged over areas north of $\approx 30^\circ$ S, is ≈ 0.54 .

The histogram indicates that Pluto has (at least) three general categories of albedo. One category has an incidence-angle-average bolometric hemispherical albedo mode of ≈ 0.1 and a relatively narrow distribution; it corresponds to the very dark southern equatorial terrains. Cthulhu and Krun, the very dark terrains to the southwest and southeast of Sputnik Planitia, respectively, have similar albedo but differ in their morphology. This suggests that their albedo may not be indicative of the process that formed these regions, but rather of subsequent processing (such as energetic radiation) or deposition (such as atmospheric hazes). Another albedo category has an incidence-angle-average bolometric hemispherical albedo mode of ≈ 0.85 and a relatively narrow distribution. Sputnik Planitia, East Tombaugh Regio, Venera Terra, and Voyager Terra are the terrains in this category. Venera and Voyager terrae are relatively near the subsolar point (solar illumination with $i = 0$),

and imperfect modeling of reflectance variation with imaging geometry may artificially increase their measured albedo. However, we are confident that both terrae have greater-than-average albedo because they are consistently brighter than surrounding areas in other images, when the subsolar point is far from the longitudes of these terrae, as Pluto rotates. Thus, Venera and Voyager terrae have very high albedos, although not quite as high as depicted in the map. The third albedo category corresponds to the remainder of Pluto’s observed surface; the incidence-angle-average bolometric hemispherical albedo mode is ≈ 0.6 , and the distribution is much broader than that of the other two categories.

The large and spatially sharp albedo difference between Sputnik Planitia and Cthulhu/Krun to its southwest/southeast suggests that processes on Pluto can effectively sort dark and bright material. One hypothesis for Pluto’s very dark southern equatorial terrains is that they are blanketed by haze from its atmosphere (e.g., Grundy et al. 2016; Moore et al. 2016; Fayolle et al. 2021). If so, deposition of dark haze material must be inhibited on southern Sputnik Planitia, and/or southern Sputnik Planitia sequesters dark haze material faster than it is deposited.

Pluto’s dramatic albedo variations with location may result in surface temperature differences of ≈ 20 K, as previously noted in Buratti et al. (2017). These albedo-induced temperature differences could significantly influence global circulation and drive cold-trapping, runaway albedo effects (e.g., Hamilton et al. 2016; Earle et al. 2018), and local aeolian phenomena. The latter possibility is yet more plausible with the consideration that extreme albedo variability sometimes occurs over very short distances. For example, Cthulhu and Krun are immediate neighbors of Sputnik Planitia. Exotic phenomena based on significant lateral heat conduction may also occur. A

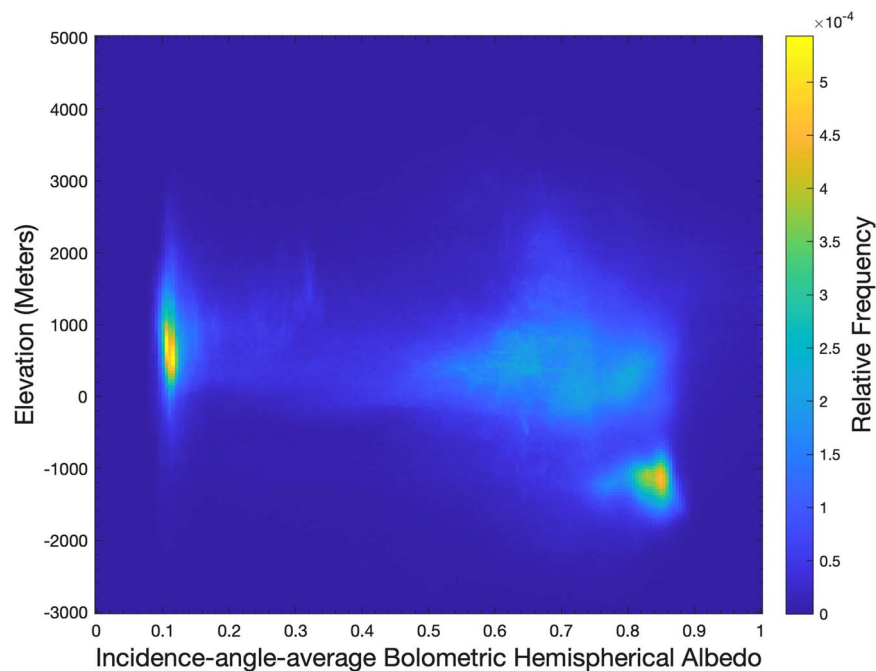


Figure 10. Albedo-topography histogram of Pluto's New Horizons encounter hemisphere. Elevation measurements are from Schenk et al. (2018). The concentration at low albedo corresponds to Cthulhu and Krun, and the concentration at low elevation and high albedo corresponds to Sputnik Planitia.

speculative hypothesis is that thermal fracturing and/or fatigue from repetitive, large temperature changes, from contact of high- and low-albedo material, could be an erosive process on Pluto. For example, colder nitrogen-ice in Tombaugh Regio, which flows on geologic timescales (e.g., McKinnon et al. 2016; Moore et al. 2016; Umurhan et al. 2017), could flow into contact with hotter Cthulhu and Krun and lower their surface temperature via nitrogen-ice sublimation, which would reexpose the lower-albedo surface so it can subsequently be reheated by solar insolation. Thermal spallation is a known weathering process on Earth (e.g., McFadden et al. 2005; Collins & Stock 2016) and elsewhere (e.g., Molaro et al. 2020).

Some simulations of Pluto's thermal evolution and/or atmospheric circulation considered lower albedos for Pluto's highest-albedo terrains than the values determined in this research (e.g., Earle et al. 2018). Other simulations used albedos that are approximately consistent with the low uncertainty estimate of the best fit for Sputnik Planitia (e.g., Bertrand et al. 2020), and some simulations explored a broad range of albedos (e.g., Johnson et al. 2021). General implications of a higher albedo than that simulated may include reduced volatile transport, a greater possibility of collapse from a global to local atmosphere (e.g., Hofgartner et al. 2019), and stronger albedo feedbacks. However, any such changes may be smaller if the effective emissivity is also lower than that assumed in simulations. An emissivity much lower than unity was previously inferred for Triton (e.g., 0.46 ± 0.16 ; Hillier et al. 1991), and Pluto's compositionally similar surface may also have an effective emissivity well below unity.

The topography of Pluto's New Horizons encounter hemisphere was measured using stereogrammetry (Schenk et al. 2018). Figure 10 is an albedo-topography histogram of Pluto's encounter hemisphere. Sputnik Planitia is distinct as a concentration at high albedo and low elevation with relatively narrow distributions in both albedo and topography. We attribute its distinct albedo-topography distribution to an

expansive, deep basin (Schenk et al. 2018) that is partially filled with nitrogen-rich ice (e.g., Protopapa et al. 2017) and ongoing albedo-topography volatile-ice feedbacks (e.g., Bertrand & Forget 2016; Umurhan et al. 2017), which result in relatively uniform brightness and elevation. Topographic lows, however, do not invariably have very high albedo surfaces. For example, a valley northwest of Sputnik Planitia (Figure 1), with surface elevations lower than that of the ice sheet, by greater than a kilometer at many locations (Schenk et al. 2018), has incidence-angle-average bolometric hemispherical albedos of only ≈ 0.2 – 0.4 . The relatively low albedos likely inhibit nitrogen condensation: an ≈ 2 – 3 km deep valley at $\approx 30^\circ$ N, with thermal inertia > 800 tiu and emissivity ≈ 0.9 , is predicted to have a surface temperature high enough to prevent nitrogen condensation, throughout a Pluto year, when the bolometric hemispherical albedo is $\lesssim 0.4$ (for nitrogen-ice thermal parameters similar to those in Reference Case A from Johnson et al. 2021). Eastern Cthulhu (approximately half of Cthulhu is included in the topographic map) has a relatively broad topographic distribution; unlike Sputnik Planitia, it is not topographically distinct.

Although Cthulhu is among Pluto's darkest terrains, it is interesting to note that Cthulhu may have a greater albedo in the LORRI panchromatic filter (incidence-angle-average hemispherical albedo of ≈ 0.10 ; Table 3) than Kuiper Belt object (486958) Arrokoth (≈ 0.06 ; Hofgartner et al. 2021). The estimated uncertainty of both measurements is $\approx \pm 0.02$, so, considering the uncertainties, there may be no difference. An approximate bolometric albedo of Arrokoth based on New Horizons LORRI and MVIC observations has not been determined, hence our comparison of LORRI albedos. The brightest areas of Arrokoth may have an albedo similar to or lower than that of best-fit Cthulhu. Furthermore, Cthulhu is significantly redder than Arrokoth; dark-red areas of Cthulhu away from its boundary have a spectral slope of $50.1\% \pm 0.1\%$ per 100 nm at 550 nm (Olkin et al. 2021), compared to

27% \pm 3% for average Arrokoth (Grundy et al. 2020). If dark-red material on both Pluto and Arrokoth was produced by chemical modification by energetic radiation (e.g., Grundy et al. 2016, 2020), the color (and possibly albedo) difference(s) suggests that they had different initial compositions or radiation-processing histories, possibly due to deposition of atmospheric products on Pluto, atmospheric shielding on Pluto, and/or an age difference.

7. Conclusions

The incidence-angle-average bolometric hemispherical albedos (local energy balance albedos, equal to one minus absorption) of Pluto's Cthulhu and Sputnik Planitia are 0.12 ± 0.01 and 0.80 ± 0.06 , respectively. Bolometric albedo was approximated using best-fit lunar-Lambert photometric functions for New Horizons LORRI panchromatic and MVIC panchromatic, blue, and red filter observations of Pluto. The variation of bolometric hemispherical albedo with incidence angle of each terrain is shown in Figure 6; the bolometric hemispherical albedo of both terrains increases by $> 30\%$ from 0° to 90° incidence. The bolometric Bond albedos of Cthulhu and Sputnik Planitia (global energy balance albedos, if each terrain, hypothetically, covered an entire sphere) are 0.12 ± 0.01 and 0.80 ± 0.07 , respectively. Uncertainties are estimates based on scatter from different photometric functional forms (dominant uncertainty).

An incidence-angle-average bolometric hemispherical albedo map of Pluto was produced and is shown in Figure 7 (equirectangular projection) and Figure 8 (north polar stereographic projection). The map was produced using the best-fit lunar-Lambert photometric functions for Cthulhu and Sputnik Planitia as representative of Pluto's extreme low- and high-reflectance regions and by approximating intermediate-reflectance regions as a linear combination of these two extremes. Pluto has three general albedo categories: (1) very low albedo southern equatorial terrains, including Cthulhu; (2) high-albedo terrains, which constitute most of Pluto's surface; and (3) very high albedo terrains, including Sputnik Planitia, East Tombaugh Regio, Venera Terra, and Voyager Terra. The incidence-angle-average bolometric hemispherical albedo of Pluto, spatially averaged over areas north of $\approx 30^\circ$ S (much of Pluto's southern hemisphere was in winter darkness (polar night) during the New Horizons encounter), is ≈ 0.54 .

Pluto has extraordinary albedo variability with location that is also spatially sharp at some places, such as at the boundary between Cthulhu and Sputnik Planitia. The albedo variations may result in surface temperature differences of ≈ 20 K.

Data Availability

The resultant albedo map will be archived through the NASA Planetary Data System (PDS) Small Bodies Node (SBN) and will be available at doi:10.26007/62b6-ya11.

Acknowledgments

We thank the entire NASA New Horizons team for enabling this research. We also thank Michael Hicks (retired from the Jet Propulsion Laboratory) for discussions during conceptualization of this research and two anonymous reviewers for their service and constructive comments. Financial support from the NASA New Frontiers Data Analysis Program (NFDAP) is

gratefully acknowledged (grant No. 80NSSC22K1118). Part of this research was carried out at the Jet Propulsion Laboratory, California Institute of Technology, under a contract with the National Aeronautics and Space Administration. This research has made use of the USGS Integrated Software for Imagers and Spectrometers (ISIS) and free and open-source QGIS software.

Appendix Similar Limits of Lunar-Lambert and Hapke Photometric Functions

Recall from Section 3 that the lunar-Lambert photometric function is

$$\frac{I}{F} = A \frac{f(\alpha) \cos i}{\cos i + \cos e} + (1 - A) \cos i. \quad (\text{A1})$$

Its parameters are defined in Sections 2 and 3. As discussed, the first term is the lunar (Lommel–Seeliger) function, which is an analytic solution to the equations of radiative transfer for single scattering. The second term is the Lambert function, which describes perfectly diffuse scattering, an approximation of multiple scattering since numerous scatterings approximately randomize the propagation direction of any given photon. The relative contribution of multiple scattering to total reflectance generally decreases with decreasing total reflectance, since if the average fraction of energy scattered (i.e., not absorbed) by each successive scattering is w (called single-scattering albedo), the energy scattered from all n th scatterings is $\propto w^n$. Thus, since $0 \leq w \leq 1$, the multiple-scattering relative contribution decreases faster than the single-scattering relative contribution as w decreases. Therefore, the relative contribution of the Lambert term is expected to decrease with decreasing total reflectance. Indeed, this trend is observed among worlds throughout the solar system (e.g., Buratti et al. 2017 and references therein).

The isotropic multiple-scattering approximation is a photometric function developed by Hapke (e.g., Hapke 2012). Several variants of the function to model effects of shadow hiding, coherent backscatter, macroscopic roughness, and porosity, among other considerations, have also been published (Hapke 2012 and references therein). For the purpose of comparison in this appendix, we ignore those enhancements; here, ‘‘Hapke photometric function’’ refers to the isotropic multiple-scattering approximation that is common to all variants. The Hapke photometric function is

$$\frac{I}{F} = \frac{w}{4} \left(\frac{\cos i}{\cos i + \cos e} \right) (p(\alpha) + M(i, e, w)), \quad (\text{A2})$$

where w is single-scattering albedo as defined above, $p(\alpha)$ is the average single-scattering phase function, M describes multiple scattering, and the other parameters are consistent with the notation for the lunar-Lambert function. Both the lunar-Lambert and Hapke photometric functions are a linear combination of single- and multiple-scattering terms, and they have the same single-scattering term if $Af(\alpha) = wp(\alpha)/4$. The equation for M is $M(i, e, w) = H(i, w)H(e, w) - 1$, where H is the Ambartsumian–Chandrasekhar H -function, which can be approximated by (e.g., Hapke 2012)

$$H(x, y) = \frac{1 + 2 \cos x}{1 + 2 \cos x \sqrt{1 - y}}. \quad (\text{A3})$$





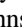

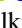



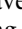
As w approaches its lower limit of zero, $H(i, w)$ and $H(e, w)$ both approach unity and $M(i, e, w)$ approaches zero: the relative contribution of the single-scattering term of the Hapke

function increases, just as occurs for the lunar-Lambert function in the limit of low reflectance. As w approaches its upper limit of unity,

$$\frac{I}{F} \rightarrow \frac{p(\alpha)}{4} \left(\frac{\cos i}{\cos i + \cos e} \right) + \frac{\cos i}{2} + \frac{(\cos i)^2 \cos e}{\cos i + \cos e}. \quad (\text{A4})$$

In this limit, the Hapke photometric function has a term $\propto \cos i$, like the multiple-scattering term of the lunar-Lambert photometric function, whose relative contribution increases as reflectance increases. The Hapke photometric function has an additional term and thus is certainly not identical to the lunar-Lambert function, but the two functions are similar in this limit. We conclude that the lunar-Lambert and Hapke photometric functions are similar in the limits of single scattering and low and high albedo.

ORCID iDs

Jason D. Hofgartner  <https://orcid.org/0000-0002-6517-3864>
 Bonnie J. Buratti  <https://orcid.org/0000-0002-5901-4875>
 Ross A. Beyer  <https://orcid.org/0000-0003-4503-3335>
 Will M. Grundy  <https://orcid.org/0000-0002-8296-6540>
 Perianne E. Johnson  <https://orcid.org/0000-0001-6255-8526>
 Tod R. Lauer  <https://orcid.org/0000-0003-3234-7247>
 Catherine B. Olkin  <https://orcid.org/0000-0002-5846-716X>
 John R. Spencer  <https://orcid.org/0000-0003-4452-8109>
 S. Alan Stern  <https://orcid.org/0000-0001-5018-7537>
 Harold A. Weaver  <https://orcid.org/0000-0003-0951-7762>
 Leslie A. Young  <https://orcid.org/0000-0002-7547-3967>

References

Bertrand, T., & Forget, F. 2016, *Natur*, 540, 86
 Bertrand, T., Forget, F., White, O., et al. 2020, *JGRE*, 125, e06120
 Buie, M. W., Grundy, W. M., Young, E. F., Young, L. A., & Stern, S. A. 2010, *AJ*, 139, 1128
 Buratti, B., & Veverka, J. 1983, *Icar*, 55, 93
 Buratti, B., & Veverka, J. 1984, *Icar*, 58, 254
 Buratti, B. J. 1984, *Icar*, 59, 392

Buratti, B. J., Hicks, M. D., Dalba, P. A., et al. 2015, *ApJL*, 804, L6
 Buratti, B. J., Hicks, M. D., Kramer, E., et al. 2021, *GeoRL*, 48, e92562
 Buratti, B. J., Hofgartner, J. D., Hicks, M. D., et al. 2017, *Icar*, 287, 207
 Cheng, A. F., Weaver, H. A., Conard, S. J., et al. 2008, *SSRv*, 140, 189
 Colina, L., Bohlin, R. C., & Castelli, F. 1996, *AJ*, 112, 307
 Collins, B. D., & Stock, G. M. 2016, *NatGe*, 9, 395
 Earle, A. M., Binzel, R. P., Young, L. A., et al. 2018, *Icar*, 303, 1
 Fayolle, M., Quirico, E., Schmitt, B., et al. 2021, *Icar*, 367, 114574
 Gladstone, G. R., Stern, S. A., Ennico, K., et al. 2016, *Sci*, 351, aad8866
 Grundy, W. M., Binzel, R. P., Buratti, B. J., et al. 2016, *Sci*, 351, aad9189
 Grundy, W. M., Bird, M. K., Britt, D. T., et al. 2020, *Sci*, 367, aay3705
 Hamilton, D. P., Stern, S. A., Moore, J. M., et al. 2016, *Natur*, 540, 97
 Hapke, B. 2012, *Theory of Reflectance and Emittance Spectroscopy* (Cambridge: Cambridge Univ. Press)
 Hillier, J., Helfenstein, P., Verbiscer, A., & Veverka, J. 1991, *JGR*, 96, 19203
 Hillier, J. H., Buratti, B. J., Hofgartner, J. D., et al. 2021, *PSJ*, 2, 11
 Hofgartner, J. D., Buratti, B. J., Benecchi, S. D., et al. 2021, *Icar*, 356, 113723
 Hofgartner, J. D., Buratti, B. J., Devins, S. L., et al. 2018, *Icar*, 302, 273
 Hofgartner, J. D., Buratti, B. J., Hayne, P. O., & Young, L. A. 2019, *Icar*, 334, 52
 Howett, C. J. A., Parker, A. H., Olkin, C. B., et al. 2017, *Icar*, 287, 140
 Johnson, P. E., Young, L. A., Protopapa, S., et al. 2021, *Icar*, 356, 114070
 Kutsop, N. W., Hayes, A. G., Buratti, B. J., et al. 2021, *PSJ*, 2, 91
 Lauer, T. R., Spencer, J. R., Bertrand, T., et al. 2021, *PSJ*, 2, 214
 McEwen, A. S. 1986, *JGR*, 91, 8077
 McFadden, L. D., Eppes, M. C., Gillespie, A. R., & Hallet, B. 2005, *GSAB*, 117, 161
 McKinnon, W. B., Nimmo, F., Wong, T., et al. 2016, *Natur*, 534, 82
 Molaro, J. L., Walsh, K. J., Jawin, E. R., et al. 2020, *NatCo*, 11, 2913
 Moore, J. M., McKinnon, W. B., Spencer, J. R., et al. 2016, *Sci*, 351, 1284
 Morison, A., Labrosse, S., & Choblet, G. 2021, *Natur*, 600, 419
 Nimmo, F., Umurhan, O., Lisse, C. M., et al. 2017, *Icar*, 287, 12
 Olkin, C. B., Ennico, K., & Spencer, J. 2017, *NatAs*, 1, 663
 Olkin, C. B., Howett, C. J. A., Protopapa, S., et al. 2021, in *The Pluto System After New Horizons*, ed. S. A. Stern et al. (Tucson, AZ: Univ. Arizona Press), 147
 Protopapa, S., Grundy, W. M., Reuter, D. C., et al. 2017, *Icar*, 287, 218
 Protopapa, S., Olkin, C. B., Grundy, W. M., et al. 2020, *AJ*, 159, 74
 Reuter, D. C., Stern, S. A., Scherrer, J., et al. 2008, *SSRv*, 140, 129
 Schenk, P. M., Beyer, R. A., McKinnon, W. B., et al. 2018, *Icar*, 314, 400
 Squyres, S. W., & Veverka, J. 1982, *Icar*, 50, 115
 Stern, S. A., Bagenal, F., Ennico, K., et al. 2015, *Sci*, 350, aad1815
 Umurhan, O. M., Howard, A. D., Moore, J. M., et al. 2017, *Icar*, 287, 301
 Verbiscer, A. J., Helfenstein, P., Porter, S. B., et al. 2022, *PSJ*, 3, 95
 Weaver, H. A., Buie, M. W., Buratti, B. J., et al. 2016, *Sci*, 351, aae0030
 Weaver, H. A., Cheng, A. F., Morgan, F., et al. 2020, *PASP*, 132, 035003